Delft University of Technology

A nonlocal material point method for the simulation of large deformation problems in brittle soils

González Acosta, José L.; Mánica, Miguel A.; Vardon, Philip J.; Hicks, Michael A.; Gens, Antonio

Research Paper

A nonlocal material point method for the simulation of large deformation problems in brittle soils

José L. González Acosta [a,*], Miguel A. Mánica [b], Philip J. Vardon [c], Michael A. Hicks [c], Antonio Gens [d]

[a] *Geosciences and Material Technology, Energy and Materials Transition, TNO, Utrecht, The Netherlands*
[b] *Institute of Engineering, National Autonomous University of Mexico, Mexico City, Mexico*
[c] *Faculty of Civil Engineering and Geosciences, Delft University of Technology, Delft, The Netherlands*
[d] *Department of Civil and Environmental Engineering, Universitat Politècnica de Catalunya, Barcelona Tech - CIMNE, Barcelona, Spain*

ABSTRACT

This paper investigates the implementation of a nonlocal regularisation of the material point method to mitigate mesh-dependency issues for the simulation of large deformation problems in brittle soils. The adopted constitutive description corresponds to a simple elastoplastic model with nonlinear strain softening. A number of benchmark simulations, assuming static and dynamic conditions, were performed to show the importance of regularisation, as well as to assess the performance and robustness of the implemented nonlocal approach. The relevance of addressing stress oscillation issues, due to material points crossing element boundaries, is also demonstrated. The obtained results provide relevant insights into brittle materials undergoing large deformations within the MPM framework.

1. Introduction

In the field of geotechnical engineering, particularly in the study of large deformation problems, the material point method (MPM) has emerged as a reliable technique for generating accurate and objective results. Established from the same principles as the finite element method (FEM), MPM inherits many of the mathematical features of FEM, and facilitates the computation of large deformations by adding an additional step in the solution process. The standard MPM computational steps are depicted in Fig. 1. While Fig. 1a and b show the standard FEM solution steps (that is, nodal solution and mesh deformation), Fig. 1c illustrates the fundamental MPM step, in which the numerical mesh is reset to its original position while the material points remain in their last location. Subsequently, an allocation procedure is implemented to establish the new location of each material point relative to the undeformed mesh (indicated with bold dashed lines). Extensive research has substantiated the versatility of MPM in simulating a diverse array of problems, including, but not limited to, soil–structure interaction (González Acosta et al., 2021a; Lian et al., 2011; Phuong et al., 2016), the triggering and post-failure behaviour of landslides (González Acosta et al., 2021b; Troncone et al., 2022; Yerro et al., 2019), earthquake phenomena (Kohler et al., 2022), CPT penetration (Martinelli and Galavi, 2021), and unsaturated behaviour (Yerro et al., 2022). However, just as MPM possesses many of the FEM

advantages, it also shares many of its limitations, such as volumetric locking, which often occurs during the simulation of materials with low compressibility, or the hourglass effect, which is linked to the utilisation of low-order elements. Similarly, it is well-known that the simulation of the softening response in brittle materials leads to non-objective FEM results with a pathological dependence on the adopted mesh (Sluys and de Borst, 1992; de Borst et al., 1993; Mánica et al., 2018) and numerical convergence issues (Summersgill et al., 2017; Mánica et al., 2022a; Cui et al., 2023). Deformation in simulations of brittle materials localises in shear bands with a thickness of a single element and, therefore, vanishing energy dissipation is attained as the size of the elements is reduced (Bažant and Pijaudier-Cabot, 1988), which is physically inadmissible. The source of these numerical difficulties is the absence of an internal length scale in classical continuum formulations representing the microstructure of the material, which in reality controls the size of the localisation region (Desrues and Viggiani, 2004).

Solutions have been developed to address issues related to volumetric locking (Coombs et al., 2018; González Acosta et al., 2019) or the hourglass effect (Zhang et al., 2017) within the MPM framework. Regarding mesh dependency issues, different approaches have been proposed and implemented in conventional FEM formulations, usually known as regularisation techniques, such as enriched continua with

---

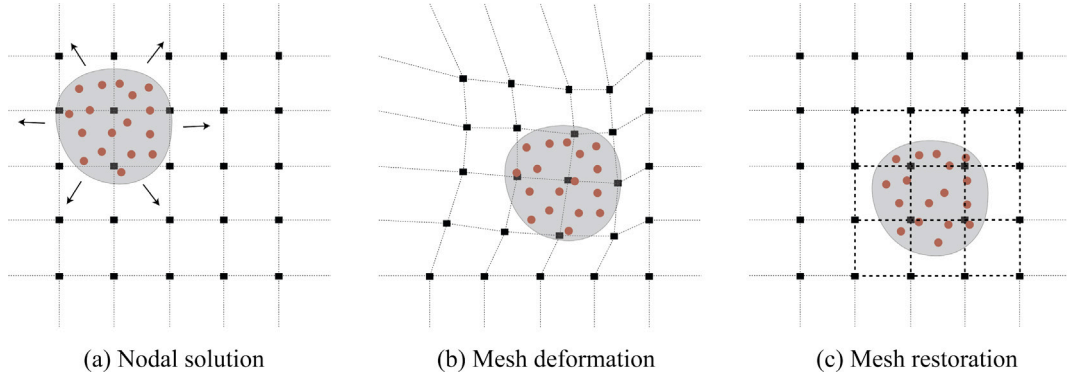(a) Nodal solution   (b) Mesh deformation   (c) Mesh restoration

Fig. 1. Solution steps in the MPM.

microstructure (Tejchman and Bauer, 2005; Khoei and Karimi, 2008), gradient models (Anand et al., 2012; Frédéric et al., 2021), or nonlocal models (Galavi and Schweiger, 2009; Summersgill et al., 2017; Mánica et al., 2018; Cui et al., 2023). However, their implementation in MPM formulations remains limited. Some authors have demonstrated that nonlocal regularisation in MPM can have a significant impact on the obtained results (Burghardt et al., 2012; Goodarzi and Rouainia, 2017). Nevertheless, a comprehensive study on the use of nonlocal models in MPM is still missing in the literature.

In this paper, an investigation is conducted regarding the implementation of a nonlocal regularisation into the MPM framework, for the simulation of large deformation problems in quasi-brittle materials. Initially, the mathematical framework of the adopted MPM formulation is described. Subsequently, the considered strain-softening elastoplastic model for the constitutive description of quasi-brittle geomaterials is presented, as well as its nonlocal extension within the MPM formulation. Finally, a series of simple boundary value problems (BVP) are analysed to demonstrate the effect and importance of the implemented nonlocal regularisation for the simulation of softening materials in the MPM.

2. MPM formulation

2.1. Conventional MPM

The exploration of the advantages of using a nonlocal formulation is performed by examining a range of static and dynamic problems. Although both formulations have been broadly elaborated by numerous authors, such as Beuth et al. (2011), Guilkey and Weiss (2003) and Wang et al. (2016), they are delineated here for completeness. For the dynamic MPM formulation, the implicit framework is used. Based on the principle of virtual work (i.e. $\Pi = W^{\text{int}} - W^{\text{ext}}$), the equation of implicit equilibrium is

$$\Pi = \frac{1}{2} \int_V \boldsymbol{\epsilon}^{\text{T}} \mathbf{D} \boldsymbol{\epsilon} \mathrm{d}V - \int_V \mathbf{u}^{\text{T}} \rho \vec{\mathbf{b}} \mathrm{d}V - \int_\Gamma \mathbf{u}^{\text{T}} \vec{\tau} \mathrm{d}\Gamma = 0 \tag{1}$$

where $\mathbf{D}$ is the stiffness matrix, $\mathbf{b}$ is the vector of body forces, $\mathbf{u}$ and $\boldsymbol{\epsilon}$ are the actual displacement and strain fields describing the state of the system, ρ is the material density, τ is the vector of boundary loads, and V and Γ are the body volume and boundary, respectively. Then, by following standard finite element discretisation procedures (Bathe, 1995), and by evaluating $\delta\Pi = 0$ (i.e. the first variation of the potential energy is equal to zero for any admissible virtual displacement) with respect to the displacements, the equation of equilibrium can be written as

$$\int_V \delta\boldsymbol{\epsilon}^{\text{T}} \mathbf{D} \boldsymbol{\epsilon} \mathrm{d}V = + \int_V \delta\mathbf{u}^{\text{T}} \rho \vec{\mathbf{b}} \mathrm{d}V + \int_\Gamma \delta\mathbf{u}^{\text{T}} \vec{\tau} \mathrm{d}\Gamma = 0 \tag{2}$$

where $\delta\boldsymbol{\epsilon}$ and $\delta\mathbf{u}$ represent the virtual displacement and virtual strain, respectively, and are used as test functions. Then, by employing shape

functions interpolation, such as $\delta\mathbf{u} = \mathbf{N}\delta\overline{\mathbf{u}}$ and $\delta\boldsymbol{\epsilon} = \mathbf{B}\delta\overline{\mathbf{u}}$, where $\mathbf{N}$ and $\mathbf{B}$ are the shape functions (SFs) and strain–displacement matrices, respectively, and an incremental formulation (i.e. $\boldsymbol{\sigma} = \boldsymbol{\sigma}^0 + \mathbf{D}\boldsymbol{\epsilon}$), the following element equation is obtained:

$$\left[\sum_{i=1}^{n_{\text{mp}}} \mathbf{B}^{\text{T}}\left(\mathbf{x}_p\right) \mathbf{D}_p \mathbf{B}\left(\mathbf{x}_p\right) |\mathbf{J}| \mathrm{W}_p\right] \Delta\overline{\mathbf{u}} =$$

$$\sum_{i=1}^{n_{\text{mp}}} \rho_p \mathbf{N}^{\text{T}}\left(\mathbf{x}_p\right) \overline{\mathbf{b}} |\mathbf{J}| \mathrm{W}_p + \sum_{mp=1}^{b_{\text{mp}}} \mathbf{N}^{\text{T}}\left(\mathbf{x}_p\right) \overline{\tau} \Gamma - \sum_{i=1}^{n_{\text{mp}}} \mathbf{B}^{\text{T}}\left(\mathbf{x}_p\right) \boldsymbol{\sigma} |\mathbf{J}| \mathrm{W}_p \tag{3}$$

which can be expressed in matrix form as

$$\mathbf{K}\Delta\overline{\mathbf{u}}\big|_{\text{elem}} = \mathbf{F}^{\text{ext}}\big|_{\text{elem}} - \mathbf{F}^{\text{int}}\big|_{\text{elem}} \tag{4}$$

where $\mathbf{x}_p$ is the position of the material point p, n_{mp} and b_{mp} are the number of material points and boundary material points mp in the computational domain, $|\mathbf{J}|$ is the Jacobian determinant, $\mathbf{b}$ are the body forces, W_p is the material point weight, $\big|_{\text{elem}}$ indicates integration of all elements, and $\Delta\overline{\mathbf{u}}$ is the vector of incremental displacements as a function of the initial and final displacement (i.e. $\Delta\overline{\mathbf{u}} = \overline{\mathbf{u}}_{\text{new}} - \overline{\mathbf{u}}_{\text{old}}$, where $\overline{\mathbf{u}}_{\text{new}}$ and $\overline{\mathbf{u}}_{\text{old}}$ are the initial and final displacements, respectively). Note that, at the start of each iteration, $\overline{\mathbf{u}}_{\text{old}}$ is equal to zero, thus $\Delta\overline{\mathbf{u}} = \overline{\mathbf{u}}_{\text{new}}$. Then, to derive the dynamic time-dependent formulation, D'Alembert's principle and Newmark (1959) time-scheme methods are assumed. Through D'Alembert's principle, inertial forces are incorporated into Eq. (2) as part of the body forces, that is $\rho(\vec{\mathbf{b}} - \vec{\mathbf{a}})$ where $\mathbf{a}$ is the vector of accelerations. Newmark's time-dependent formulation, on the other hand, captures the progression of displacements, velocities, and accelerations from time t to $t + \Delta t$ as

$$\overline{\mathbf{v}}^{t+\Delta t} = \overline{\mathbf{v}}^t + 0.5\left[\overline{\mathbf{a}}^t + \overline{\mathbf{a}}^{t+\Delta t}\right] \Delta t \tag{5}$$

$$\overline{\mathbf{u}}^{t+\Delta t} = \overline{\mathbf{u}}^t + \overline{\mathbf{v}}^t \Delta t + 0.25\left[\overline{\mathbf{a}}^t + \overline{\mathbf{a}}^{t+\Delta t}\right] \Delta t^2 \tag{6}$$

where $\overline{\mathbf{u}}^{t+\Delta t}$, $\overline{\mathbf{v}}^{t+\Delta t}$ and $\overline{\mathbf{a}}^{t+\Delta t}$ denote the vectors of nodal displacements, velocities, and accelerations at time $t + \Delta t$ respectively. From Eqs. (5) and (6), the velocity and acceleration at time $t + \Delta t$ are

$$\overline{\mathbf{v}}^{t+\Delta t} = \frac{2\overline{\mathbf{u}}^t}{\Delta t} - \overline{\mathbf{v}}^t \tag{7}$$

$$\overline{\mathbf{a}}^{t+\Delta t} = \frac{4\overline{\mathbf{u}}^t}{\Delta t^2} - \frac{4\overline{\mathbf{v}}^t}{\Delta t} - \overline{\mathbf{a}}^t \; . \tag{8}$$

Finally, by substituting Eq. (8) into Eq. (2) and employing both D'Alembert's principle and Newton–Raphson iteration procedure, the equilibrium equation at the computational step k is written as

$$\overline{\mathbf{K}}^k \Delta\mathbf{u} = {}^{(k-1)}\left(\mathbf{F}^{\text{ext}} - \mathbf{F}^{\text{kin}} - \mathbf{F}^{\text{int}}\right)^{t+\Delta t} \tag{9}$$

where

$$\overline{\mathbf{K}} = \left(\mathbf{K}^t + \frac{4\overline{\mathbf{m}}^t}{\Delta t^2}\right) \tag{10}$$

$$\mathbf{F}^{\text{kin},t+\Delta t} = \overline{\mathbf{m}}^t \left(\frac{4^{(k-1)}\overline{\mathbf{u}}^t}{\Delta t^2} - \frac{4\overline{\mathbf{v}}^t}{\Delta t} - \overline{\mathbf{a}}^t \right) \tag{11}$$

$$\overline{\mathbf{m}} = \sum_{i=1}^{mp} \rho_p \mathbf{N}^{\text{T}} \left(\mathbf{x}_p \right) \mathbf{N} \left(\mathbf{x}_p \right) |\mathbf{J}| \mathbf{W}_p \tag{12}$$

2.2. Enhanced MPM

Whilst the standard MPM framework can analyse a range of large deformation problems, it is well known that issues, such as stress oscillation owing to element crossings and the use of linear-based SFs, can substantially compromise the accuracy of the simulation. This is particularly problematic when advanced constitutive descriptions are employed, in which the inaccuracies in stresses might lead to convergence problems and the failure of the simulation. To account for stress oscillation problems, an enhanced version of the MPM is considered, namely DM-GC MPM (González Acosta et al., 2020). DM-GC MPM is a methodology in which a double mapping (DM) procedure is combined with two stress recovery techniques: the generalised interpolation material point (GIMP) method and the composite MPM (González Acosta et al., 2017). In the DM procedure, the material point stiffness contribution is mapped to the Gauss point locations using shape functions (via the nodes) for the subsequent global stiffness integration. This is achieved using standard finite element SFs as

$$\mathbf{D}_i = \sum_{p=1}^{cmp} \mathbf{N}_i(\mathbf{x}_p) \mathbf{D}_p \mathbf{W}^* \tag{13}$$

where $\mathbf{D}_i$ is the elastic matrix at the node i, cmp is the current number of material points p in the element, and $\mathbf{W}^*$ is the (dimensionless) modified material point weight ($\mathbf{W}^* = \mathbf{W}_p \frac{omp}{cmp}$, where omp is the original number of material points in the element). After the total stiffness contribution of the material points is accumulated at the nodes, it is then redistributed to the original Gauss positions as

$$\mathbf{D}_g = \sum_{i=1}^{nn} \mathbf{N}_i(\mathbf{x}_g) \mathbf{D}_i \tag{14}$$

where $\mathbf{D}_g$ is the elastic matrix at the Gauss point g, $\mathbf{N}_i(\mathbf{x}_g)$ is the nodal SF evaluated at the Gauss points, and nn is the number of nodes of the element. Note that the location of the Gauss points is the same as in the original FEM for a 2×2 integration, which is ($\pm\varrho, \pm\eta$) where $\varrho = \eta = \frac{1}{\sqrt{3}}$. Finally, by substituting Eq. (13) into Eq. (14), the stiffness at the Gauss integration point is

$$\mathbf{D}_g = \sum_{i=1}^{nn} \left(\mathbf{N}_i(\mathbf{x}_g) \sum_{p=1}^{cmp} \mathbf{N}_i(\mathbf{x}_p) \mathbf{D}_p \mathbf{W}^* \right) \tag{15}$$

which can be integrated into Eq. (3) by replacing $\mathbf{D}_p$, thus guaranteeing a smoother distribution of the stiffness within the group of elements activated by the material points. Although the incorporation of Eq. (15) into Eq. (3) improves significantly the stiffness distribution within the activated elements, the consequences of using standard FE SFs (which extend only over a single element) hinder the effectiveness of this technique. To overcome this limitation, local GIMP SFs (Charlton et al., 2017) can be incorporated into the equation. Local GIMP SFs are a variation of the original GIMP SFs proposed by Bardenhagen and Kober (2004) to reduce oscillations derived from material points crossing element boundaries. These functions are constructed by performing a convolution of standard FE SFs and a material point support domain, leading to the following set of equations:

$$\mathbf{S}_{ip} = \frac{1}{\mathbf{V}_p} \int_{\Omega_p \cap \Omega} \chi_p(\mathbf{x}_p) \mathbf{N}_i(\mathbf{x}_p) \, \mathrm{d}\mathbf{x} \tag{16}$$

$$\nabla \mathbf{S}_{ip} = \frac{1}{\mathbf{V}_p} \int_{\Omega_p \cap \Omega} \chi_p(\mathbf{x}_p) \nabla \mathbf{N}_i(\mathbf{x}_p) \, \mathrm{d}\mathbf{x} \tag{17}$$

where Ω is the problem domain, Ω_p is the material point support domain, and χ is the function delimiting the area of influence of the material point, presented originally as

$$\chi_p(\mathbf{x}_p) = \begin{cases} 1 & \text{if } \mathbf{x} \notin \Omega_p \\ 0 & \text{otherwise} \end{cases} \tag{18}$$

The local version of the original GIMP SFs, on the other hand, is created by computing the convolution of the original χ function and single-element SFs. This can be observed in Fig. 2a where two elements (E_1 and E_2) share a central node and the linear SFs N_i. When the convolution of the χ function, of length 2lp, and the SFs are computed, the standard GIMP SF (S_{ip}) are obtained (Fig. 2b). In contrast, when the convolution is computed with a single SF (Fig. 2c), the local GIMP SFs (S_{ip*}) are obtained (Fig. 2d). Therefore, by following similar steps as in the deduction of Eq. (15), the same equation can be derived but using instead the local GIMP SF, thus resulting in

$$\mathbf{D}_g = \sum_{i=1}^{nn} \left(\mathbf{N}_i(\mathbf{x}_g) \sum_{p=1}^{cmp} \mathbf{S}_{ip*}(\mathbf{x}_p) \mathbf{D}_p \mathbf{W}^* \right) . \tag{19}$$

Stiffness integration via Eq. (19) has shown to be far superior in contrast to the use of linear SFs or by introducing a mapping step using linear SFs (e.g. as proposed in Eq. (15)). Evidence of the validity of this approach can be found in González Acosta et al. (2017) and González Acosta (2020).

3. Nonlocal constitutive model for quasi-brittle materials

The nonlocal elastoplastic constitutive model described in Mánica (2018) was considered here for its implementation in the described MPM formulation. The model is intended for the simulation of argillaceous hard soils/weak rocks. Therefore, it incorporates many of the behavioural features of these materials, such as a nonlinear yield criterion, a non-associated flow rule, stiffness and strength anisotropy, rate-dependency, strain-softening, creep, and the ability to simulate objectively localised deformations by means of a nonlocal regularisation. The model has been previously implemented in the finite element code Plaxis (Bentley Systems, 2022), and its capacity to produce mesh-independent results has been demonstrated previously (Mánica et al., 2018, 2020, 2022a,b). However, for the sake of simplicity, most of the features of the model were not employed here. Therefore, as done in Mánica et al. (2020) and Romero et al. (2024), the adopted constitutive description is reduced to a simple nonlocal elastoplastic model with isotropic linear elasticity and nonlinear strain-softening.

The yield function corresponds to the following hyperbolic approximation of the Mohr–Coulomb (MC) criterion (Gens et al., 1990), which allows the tensile strength to be limited, that is usually overestimated by the classical MC criterion:

$$f = \sqrt{\frac{J_2}{f_d(\theta)} + \left(c^* + p_t \tan\phi^*\right)^2} - \left(c^* + p \tan\phi^*\right) \tag{20}$$

where c^* and ϕ^* are the asymptotic cohesion and friction angle, respectively, p_t is the isotropic tensile strength, $f_d(\theta)$ is a given function defining the shape of the criterion in the deviatoric plane, and p, J, and θ are stress invariants with their usual definitions:

$$p = \frac{1}{3} \operatorname{tr}(\boldsymbol{\sigma}) \tag{21}$$

$$J_2 = \frac{1}{2} \operatorname{tr}(\mathbf{s}^2) \tag{22}$$

$$\theta = -\frac{1}{3} \sin^{-1} \left(\frac{3\sqrt{3} \det \mathbf{s}}{2 J_2^{3/2}} \right) \tag{23}$$

where $\mathbf{s}$ is the deviatoric stress tensor, defined as $\mathbf{s} = \boldsymbol{\sigma} - p\mathbf{I}$, and $\mathbf{I}$ is the identity tensor. The shape of the yield function in the deviatoric plane is defined as van Eekelen (1980):

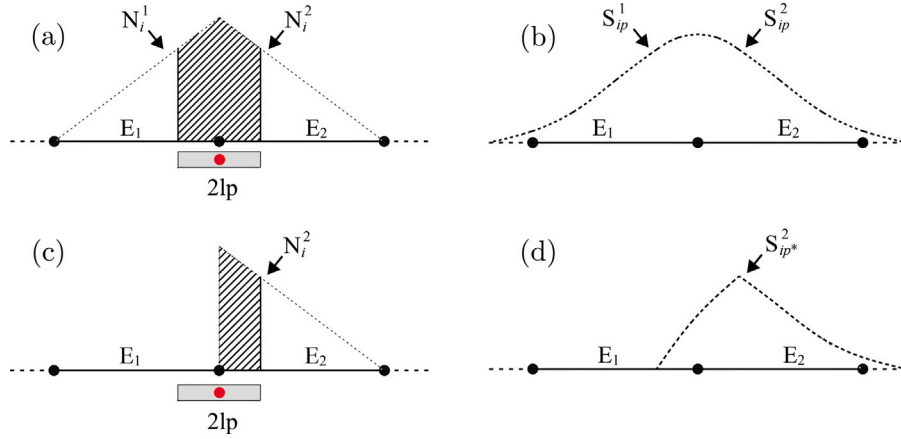$$f_d(\theta) = \alpha (1 + \beta \sin 3\theta)^n \tag{24}$$

Fig. 2. (a) Nodal FE SF and convolution with the material point support domain, (b) original GIMP SF (S_{ip}), (c) nodal FE SF and convolution with the material point support domain in a single element, and (d) local GIMP SF S_{ip^*}.

where $\beta = 0.85\alpha^{1/2}$, $n = -0.229$, and $\alpha = 0.972$ were employed.

Strain-softening is considered, driven by the evolution of the strength parameters, and it is characterised by the following exponential decay functions:

$$\tan \phi^* = \tan \phi^*_{\text{peak}} - \left(\tan \phi^*_{\text{peak}} - \tan \phi^*_{\text{res}} \right) \left[1 - \exp \left(-b_{\text{res}} \epsilon^{\text{p}}_{\text{eq}} \right) \right] \quad (25)$$

$$c^* = \left(c^*_{\text{peak}} - c^*_{\text{post}} \right) \exp \left(-b_{\text{post}} \epsilon^{\text{p}}_{\text{eq}} \right) + c^*_{\text{post}} \exp \left(-b_{\text{res}} \epsilon^{\text{p}}_{\text{eq}} \right) \quad (26)$$

$$p_{\text{t}} = \left(p_{\text{t peak}} - p_{\text{t post}} \right) \exp \left(-b_{\text{post}} \epsilon^{\text{p}}_{\text{eq}} \right) + p_{\text{t post}} \exp \left(-b_{\text{res}} \epsilon^{\text{p}}_{\text{eq}} \right) \quad (27)$$

where the subscripts *peak*, *post*, and *res* refer to peak, post-rupture, and residual conditions, respectively, b_{post} and b_{res} are parameters controlling the rate of softening, and $\epsilon^{\text{p}}_{\text{eq}}$ is a state variable defined here as

$$\epsilon^{\text{p}}_{\text{eq}} = \left(\boldsymbol{\epsilon}^{\text{p}} : \boldsymbol{\epsilon}^{\text{p}} \right)^{1/2} \quad (28)$$

where $\boldsymbol{\epsilon}^{\text{p}}$ is the plastic strain tensor. A distinction is made in Eqs. (25) to (27) between two stages of the softening process. The first one is related to a rapid degradation and breakage of interparticle bonds, i.e. a reduction of cohesion and tensile strength, up to post-rupture conditions (Burland, 1990), whose rate is defined by b_{post}. In the second one, with a slower rate b_{res}, the remaining cohesion and tensile strength vanish and the friction angle decreases as a result of the polishing and reorientation of particles in the formed failure surface (Gens, 2013).

Regarding the direction of plastic flow, a non-associated flow rule is considered, which is obtained by scaling the volumetric component of the yield function in the following way:

$$\frac{\partial g}{\partial \boldsymbol{\sigma}} = \omega \frac{\partial f}{\partial p} \frac{\partial p}{\partial \boldsymbol{\sigma}} + \frac{\partial f}{\partial J_2} \frac{\partial J_2}{\partial \boldsymbol{\sigma}} + \frac{\partial f}{\partial \theta} \frac{\partial \theta}{\partial \boldsymbol{\sigma}} \quad (29)$$

where g is the plastic potential function and ω is a parameter controlling the amount of plastic volumetric deformation.

3.1. Nonlocal extension

In general, a nonlocal model is one where the behaviour of a given point in the material depends not only on its state, but it also depends on the state of neighbouring points. If $F(\mathbf{x})$ is some given local field within a body of volume V, its nonlocal version $\bar{F}(\mathbf{x})$ can be written as

$$\bar{F}(\mathbf{x}) = \int_V w(\mathbf{x}, \boldsymbol{\xi}) F(\boldsymbol{\xi}) d\boldsymbol{\xi} \quad (30)$$

where w is a weighting factor controlling the relative importance of neighbouring points as a function of its position ($\boldsymbol{\xi}$) relative to the position of the point under consideration ($\mathbf{x}$). Usually, the radial

distance between them $\|\mathbf{x} - \boldsymbol{\xi}\|$ is assumed, and w is defined in the following normalised form to prevent modifying a uniform field:

$$w(\mathbf{x}, \boldsymbol{\xi}) = \frac{w_0 (\|\mathbf{x} - \boldsymbol{\xi}\|)}{\int_V w_0 (\|\mathbf{x} - \boldsymbol{\zeta}\|)} d\boldsymbol{\zeta} . \quad (31)$$

Different nonlocal models are obtained depending on the variable, or variables, that are assumed nonlocal. In the context of nonlocal plasticity models, different alternatives have been studied. For instance, stress or elastic strains (Eringen, 1981), total strains (Eringen, 1983), or plastic strains (Bažant and Lin, 1988) have been considered as the nonlocal fields. However, under certain conditions, these formulations might exhibit unwanted effects such as stress looking, vanishing energy dissipation, or localisation into a zone of vanishing volume (Bažant and Jirásek, 2002). Improved results have been obtained by assuming as nonlocal the scalar state variable controlling the softening process (Galavi and Schweiger, 2010; Summersgill et al., 2017; Mánica et al., 2018; Singh et al., 2021). Therefore, the nonlocal extension of the described elastoplastic model (Section 3) is obtained replacing $\epsilon^{\text{p}}_{\text{eq}}$ by the following nonlocal counterpart:

$$\bar{\epsilon}^{\text{p}}_{\text{eq}}(\mathbf{x}) = \int_V w(\mathbf{x}, \boldsymbol{\xi}) \epsilon^{\text{p}}_{\text{eq}}(\boldsymbol{\xi}) d\boldsymbol{\xi} . \quad (32)$$

Furthermore, a Gaussian function has been historically employed to characterise w_0 (see e.g. Bažant and Pijaudier-Cabot, 1988). However, as has been extensively demonstrated (Mánica et al., 2018; Summersgill et al., 2017; Monforte et al., 2019; Singh et al., 2021; Gao et al., 2022), an enhanced performance is obtained with the following function proposed by Galavi and Schweiger (2010):

$$w_0 = \frac{\|\mathbf{x} - \boldsymbol{\xi}\|}{l_{\text{s}}} \exp \left[- \left(\frac{\|\mathbf{x} - \boldsymbol{\xi}\|}{l_{\text{s}}} \right)^2 \right] \quad (33)$$

where l_{s} is a parameter controlling the spread of the function with respect to $\|\mathbf{x} - \boldsymbol{\xi}\|$, which in turn introduces a length scale to the material behaviour controlling the size of the localisation region. The particular shape resulting from Eq. (33) (Fig. 3) prevents the concentration of plastic deformations along the forming shear band, similarly to the over-nonlocal approach (Vermeer and Brinkgreve, 1994).

The described nonlocal regularisation is implemented within the MPM framework and, therefore, Eq. (31) and (32) are replaced by the following discrete versions:

$$\bar{\epsilon}^{\text{p}}_{\text{eq} p} = \sum_{j=1}^{n_{\text{mpl}}} w_{pj} \epsilon^{\text{p}}_{\text{eq} j} \quad (34)$$

$$w_{pj} = \frac{w_0 (\|\mathbf{x}_p - \mathbf{x}_j\|)}{\displaystyle\sum_{k=1}^{n_{\text{mpl}}} w_0 (\|\mathbf{x}_p - \mathbf{x}_k\|)} \quad (35)$$
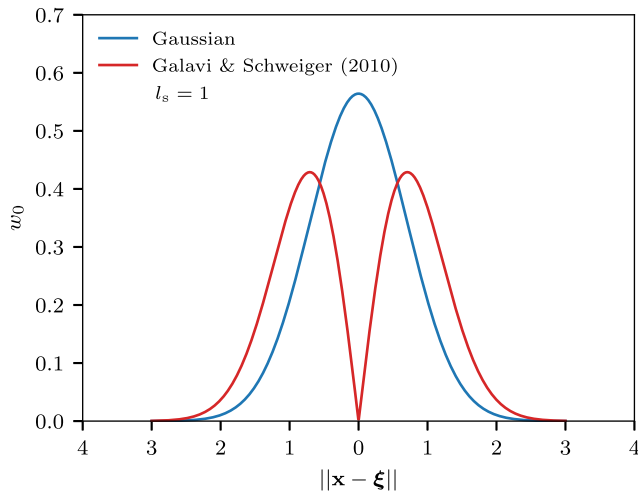
Fig. 3. Weighting function in the nonlocal approach.

Fig. 4. Search area for the identification of neighbouring points for the computation of the nonlocal state variable.

where n_{mpl} is the number of material points considered in the computation of the nonlocal state variable. Theoretically, n_{mpl} should be equal to the total number of material points in the simulation, since the weights from Eq. (33) only vanish at an infinite radial distance. However, the latter is generally computationally prohibitive and the effect of neighbouring points at distances greater than $2l_s$ is negligible. Therefore, as suggested by Galavi and Schweiger (2010), only material points within an interaction radius of $2l_s$ are considered. However, unlike conventional FEM formulations, the material points, where the constitutive equations are integrated, do not have a definite position, and they can move significantly and change elements during the simulation. Therefore, for each material point, neighbouring points within the corresponding interaction radius must be continually identified for the computation of the nonlocal state variable (Eq. (34)).

The task of searching for neighbouring points, which is closely related to the nearest-neighbour search problem (Knuth, 1997), is very computationally intensive if linear search is performed, i.e. by computing the radial distance from the query point to every other point in the simulation. However, advantage can be taken from two facts inherent to the MPM: (1) that the background mesh is constructed as a regular grid and (2) that tracking of the material points within a given element is already performed. Therefore, searching for neighbouring points can be limited to the square area shown in Fig. 4, which always contains the interaction radius. For a given material point, within an element $E[i, j]$, all elements possibly containing material points within the interaction radius can be found in $E[\alpha, \beta]$, where $\alpha = i - n_{ele}, \dots, i + n_{ele}$, $\beta = j - n_{ele}, \dots, j + n_{ele}$, and n_{ele} is the number of elements in each direction of the search area (Fig. 4), computed as

$$n_{ele} = \mathrm{floor}\left(\frac{2l_s}{l_{ele}}\right) + 1 \tag{36}$$

where l_{ele} is the length of elements in the background mesh and $\mathrm{floor}()$ is a function accounting for the integer part.

The search for neighbouring points and the computation of the nonlocal state variable is performed at the beginning of each global step, and the nonlocal variable is assumed to remain constant over the step (Rolshoven, 2003). This results in an efficient and simple algorithm rendering reasonable computation times.

4. Benchmark simulations

A number of two-dimensional (2D) plane strain simulations were performed to assess the effectiveness of the nonlocal regularisation implemented in the MPM, for both the static (Eq. (4)) and dynamic (Eq. (9)) formulat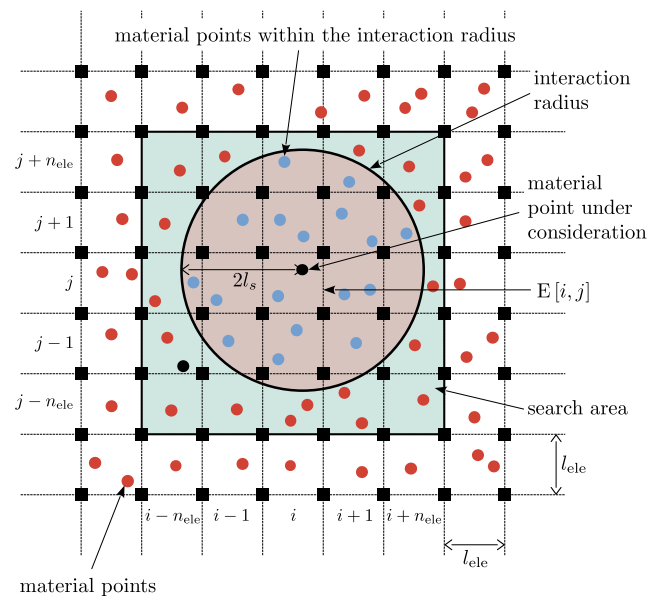ions, when softening behaviour is considered in the constitutive description; they are presented in the following sections. All simulations were performed using squared four-noded plane strain elements, with four material points evenly distributed inside the elements at the beginning of the analysis. It is important to mention that although the conventional MPM formulation (Section 2.1) was also tested, it was incapable of completing any analysis when softening was considered in the constitutive description. Numerical convergence issues are well-known in conventional FEM simulations when dealing with softening materials (Summersgill et al., 2017; Mánica et al., 2022a; Cui et al., 2023). Mathematically, this occurs because the governing partial differential equation changes locally from elliptic to hyperbolic, causing an ill-posed BVP (Read and Hegemier, 1984; Benallal and Marigo, 2007; Lu et al., 2012). These issues are accentuated in the standard MPM due to the well-known stress oscillations resulting from the movement of material points from one element to another (Tielen et al., 2017; González Acosta, 2020), preventing convergence to a steady condition as soon as softening has occurred, at the onset of plastic deformations. Therefore, in the following, results labelled as "regularised MPM" and "standard MPM" refer to the enhanced MPM formulation (Section 2.2), with and without nonlocal regularisation, respectively.

4.1. Biaxial test

The first benchmark corresponds to the simulation of the simple biaxial test shown in Fig. 5. This analysis assumes static conditions (Eq. (4)) and, therefore, inertial forces are neglected. Due to symmetry, only a quarter of the sample was represented in the analysis, with a height $h = 0.05\,\mathrm{m}$ and a width $w = 0.03\,\mathrm{m}$. Regarding boundary conditions, at the left and bottom boundaries displacements were fixed only in the normal direction, representing the symmetry axes. At the right and top boundaries, a constant confinement pressure $\sigma_3 = 100\,\mathrm{kPa}$ was applied. This value was also considered as the initial isotropic stress state assigned to all material points. Loading was applied by means of a prescribed downward vertical displacement at the top boundary, applied in fixed increments of $\Delta\delta_y = 1.0 \times 10^{-5}\,\mathrm{m}$ up to a total displacement $\delta_y = 0.00226\,\mathrm{m}$. Horizontal displacements were fixed at the top boundary in order to induce a non-homogeneous stress/strain field and, therefore, favour the onset of localisation. Table 1 summarises the

Table 1
Parameters used in the benchmark simulations performed.

| Parameter	Symbol	Units	Biaxial test	Column collapse	Foundation
Young's modulus	E	kPa	20,000	10,000	50,000
Poisson's ratio	v	–	0.2	0.35	0.45
Initial asymptotic friction angle	ϕ_{ini}^*	°	20	20	20
Peak asymptotic friction angle	ϕ_{peak}^*	°	20	20	20
Residual friction angle	ϕ_{res}^*	°	15	15	15
Initial asymptotic cohesion	c_{ini}^*	kPa	200	100	100
Post-rupture asymptotic cohesion	c_{post}^*	kPa	0	0	0
Initial tensile strength	$p_{t\,ini}$	kPa	0	0	0
Post-rupture tensile strength	$p_{t\,post}$	kPa	0	0	0
Post-rupture softening rate	b_{post}	–	10	5	5
Residual softening rate	b_{res}	–	2	2	2
Non-associativity constant	ω	–	1	1	1
Density	ρ	g/cm³	–	1.6	–
Length scale parameter	l_s	m	0.01[a]	0.4[a]	0.8[a]

[a] Only applies for the regularised MPM.
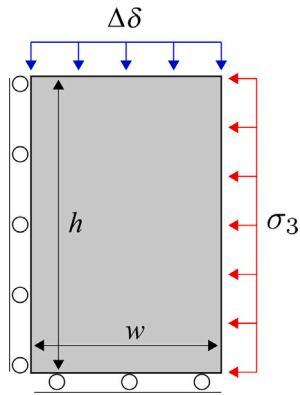
Fig. 5. Geometry and boundary conditions of the simulated biaxial test.
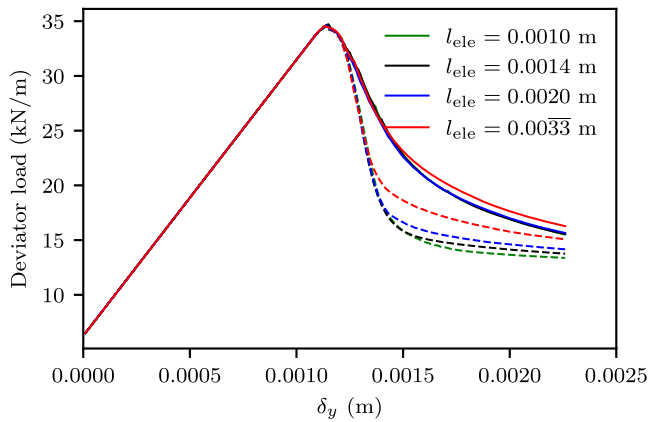

Fig. 6. Load vs. displacement curves from the biaxial test simulation obtained with the standard (dashed lines) and regularised MPM (solid lines) and for different element sizes l_{ele}.

Fig. 7. Contours of deviatoric strains and position of material points from the biaxial test simulation obtained with the standard MPM using element sizes l_{ele} of (a) 0.0033, (b) 0.002, (c) 0.0014, and (d) 0.001 m.

adopted parameters, which are similar to those employed in Mánica et al. (2018).

Analyses of the biaxial test were performed with the standard and regularised MPM and for different element sizes of the background mesh. Specifically, element sizes l_{ele} of 0.0033, 0.002, 0.0014, and 0.001 m were considered. Since a non-homogeneous stress/strain field is generated, results are assessed in terms of global measures. Fig. 6 shows the obtained deviator load vs. prescribed vertical displacement curves. The results from the standard MPM show typical mesh-dependent behaviour, with an increasingly brittle response as
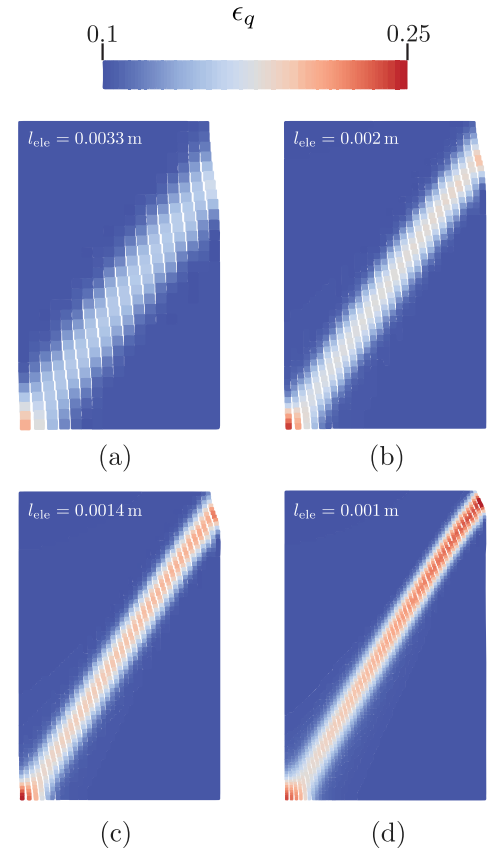
the size of elements is reduced. For the regularised MPM simulations, a length scale parameter $l_s = 0.01$ m was employed. Therefore, for all meshes, the recommendation of $l_s \geq l_{ele}$ is fulfilled (Galavi and Schweiger, 2010) so that a sufficient number of material points are considered in the nonlocal averaging. Unlike the standard MPM, practically a single curve is obtained regardless of the size of elements employed. Only the curve with $l_{ele} = 0.0033$ m lies slightly above the rest. In this regard, it is important to mention that the recommendation from Galavi and Schweiger (2010) about the minimum element size for a given l_s was derived for 15-noded triangular elements with fourth-order interpolation and 12 integration points. In the case of the four-noded linear elements used here, with four material points per element, the
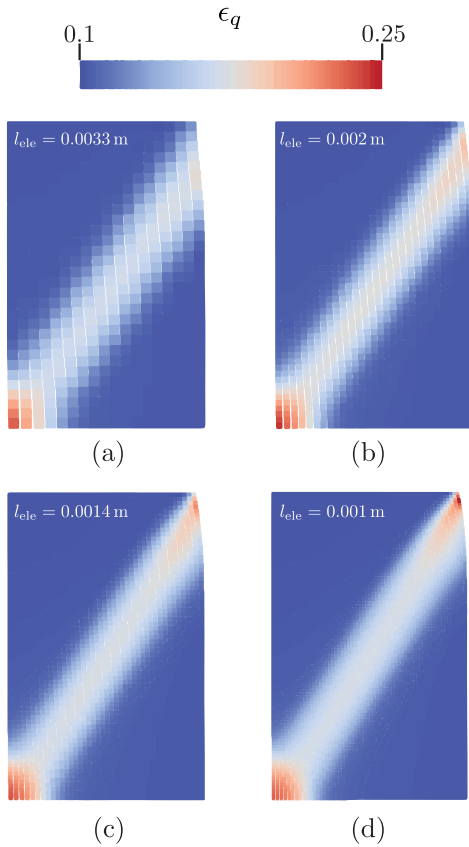
Fig. 8. Contours of deviatoric strains and position of material points from the biaxial test simulation obtained with the regularised MPM using element sizes l_{ele} of (a) 0.0033, (b) 0.002, (c) 0.0014, and (d) 0.001 m and a length scale parameter $l_s = 0.01$ m.
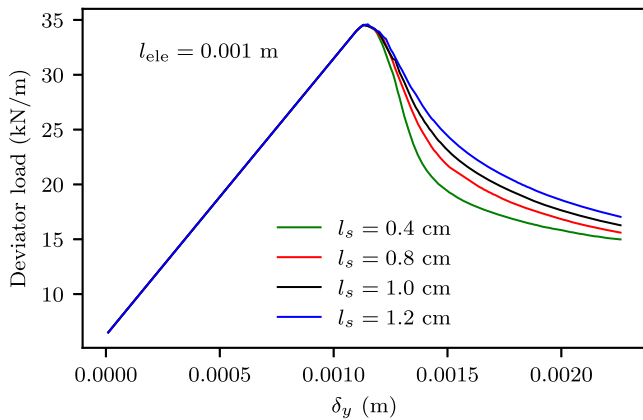

Fig. 9. Load vs. displacement curves from the biaxial test simulation obtained with the regularised MPM for different values of the length scale parameter l_s.

required minimum element size for the proper performance of the nonlocal regularisation appears to be smaller, in the order of $0.2l_s$.

Figs. 7 and 8 show the results in terms of contours of deviatoric strains ϵ_q for the standard and regularised MPM, respectively, where

$$\epsilon_q = \sqrt{\frac{2}{9}\left[(\epsilon_{xx} - \epsilon_{yy})^2 + \epsilon_{yy}^2 + \epsilon_{xx}^2\right] + \frac{1}{3}\gamma_{xy}^2}. \qquad (37)$$

The position of the material points is also depicted in the figures. In the case of the standard MPM (Fig. 7), mesh-dependent behaviour can also be identified, with the width of the formed shear band decreasing and the magnitude of deviatoric strains increasing as the size of elements
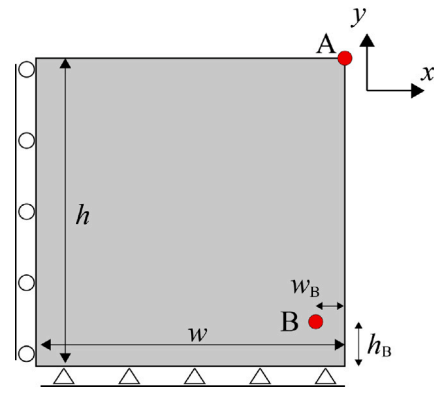

Fig. 10. Geometry and boundary conditions of the vertical cut simulation.

is reduced. On the other hand, contours from the regularised MPM (Fig. 8) show quite similar magnitudes of deviatoric strains and a similar thickness of the formed shear band, which is approximately equal to l_s, as previously reported for regularised FEM formulations using the same weighting function as Eq. (33) (Galavi and Schweiger, 2010; Mánica et al., 2018).

The parameter l_s controls the size of the localisation region, introducing a length scale to the material behaviour. If l_s is reduced, a smaller thickness of the shear band is obtained, in turn resulting in a more brittle response of the BVP, as shown in Fig. 9. Ideally, l_s should be selected to obtain a width of the localisation process similar to that occurring in the real material, which depends on its microstructure (Desrues and Viggiani, 2004). However, in most cases, this shear zone can be very small, resulting in an excessively refined mesh, exceeding conventional computational capacities, when solving practical BVPs. To overcome this issue, the softening scaling technique can be applied (Pietruszczak and Mroz, 1981; Brinkgreve, 1994; Marcher, 2003; Galavi and Schweiger, 2010; Mánica et al., 2018). It assumes that the effect of the real shear zone can be merged into a numerical shear band of a larger size, in accordance with our computational resources. Since the global post-localisation behaviour will depend on both the length scale parameter and the constitutive softening rate, they must be chosen jointly to represent a given material. However, as demonstrated by Romero et al. (2024), the latter is not a trivial task, and the derivation of parameters for a regularised simulation from conventional laboratory test results is still an open problem.

4.2. Vertical cut

The second benchmark seeks to assess the performance of the implemented nonlocal regularisation in a dynamic large deformation problem. Therefore, the formulation described by Eq. (9) is employed here. The analysis corresponds to a vertical cut where gravity is gradually increased until failure is induced. The square domain, shown in Fig. 10, is adopted, with dimensions $h = w = 3$ m. At the left boundary, null normal displacements were prescribed, while at the bottom boundary both vertical and horizontal displacement components were fixed. The employed parameters are shown in Table 1; they are similar to those used in the biaxial test, although some modifications were made to obtain a well-defined failure mechanism for this BVP. A null initial stress state was considered throughout the domain, and loading was applied by increasing gravity in the y direction in increments of $\Delta g = 0.1$ g every 0.001 s, reaching a maximum value of $g_{max} = 60$ g at $t = 0.6$ s. From this point onward, gravity was maintained constant and the simulation was continued up to $t = 0.75$ s to allow the evolution of the formed failure mechanism. For an in-depth analysis, two points, labelled A and B, are identified in the domain (Fig. 10). Point A, located at the top-right corner, is used to monitor displacements over time.
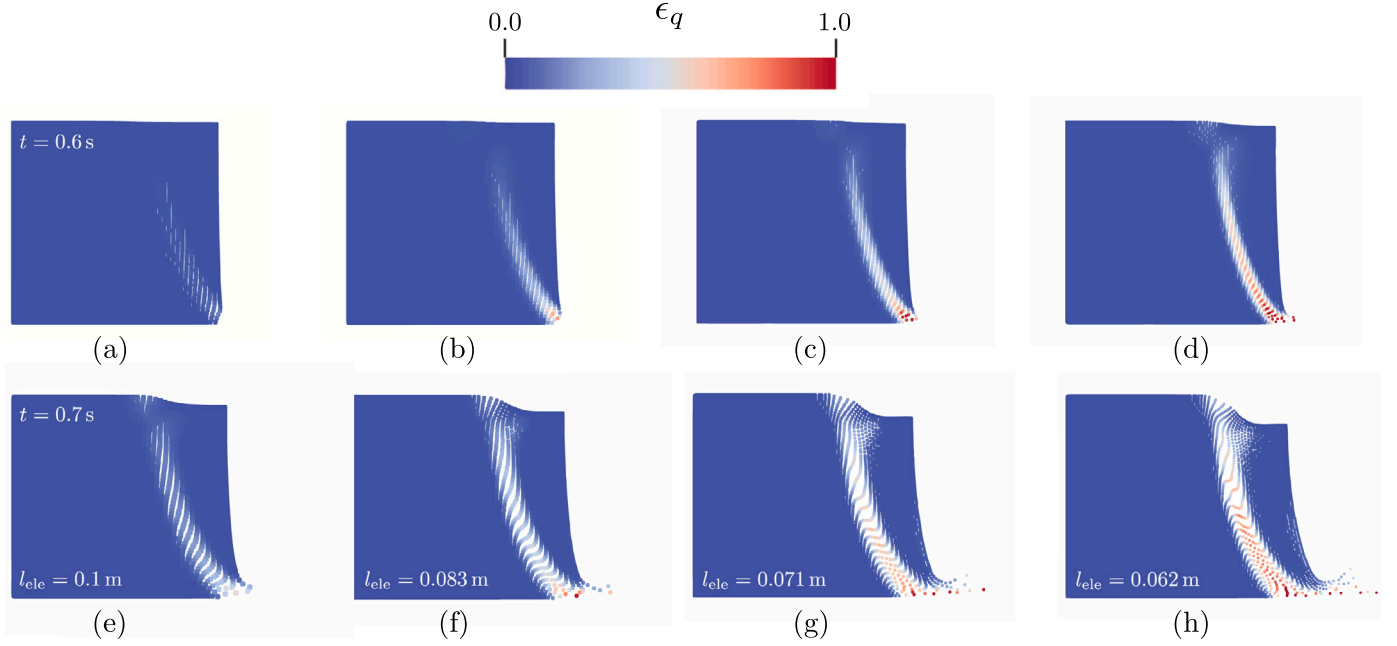
Fig. 11. Contours of normalised deviatoric strains and position of material points from the vertical cut simulation obtained with the standard MPM, for times t of 0.6 and 0.7 s, using element sizes l_{ele} of (a,e) 0.1, (b,f) 0.083, (c,g) 0.071, and (d,h) 0.062 m.
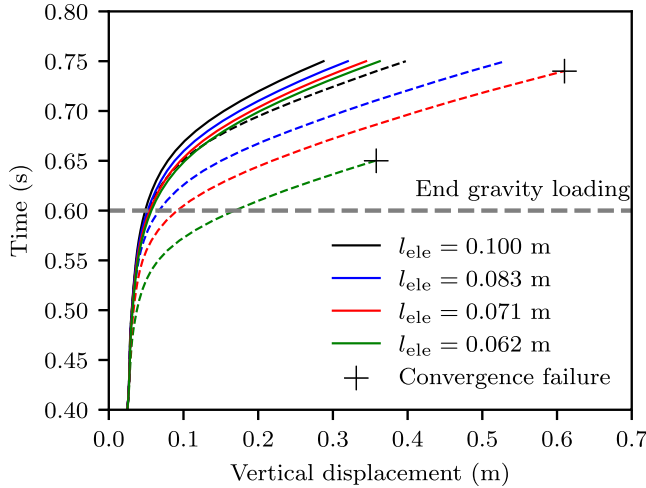

Fig. 12. Evolution of displacement at point A from the vertical cut simulation obtained with the standard (dashed lines) and regularised (solid lines) MPM and for different element sizes l_{ele}.

Point B, located at a distance from the bottom-right corner of $h_B = 0.34$ and $w_B = 0.22$ m, is used to track the evolution of deviatoric stresses close to the region where the failure mechanism initiates.

Fig. 11 shows the progression of failure, in terms of contours of deviatoric strains (normalised with respect to the corresponding maximum value) and the position of the material points, for $t = 0.6$ s (Fig. 11a to d) and $t = 0.7$ s (Fig. 11e to h) and for different element sizes of the background mesh. Again, the mesh-dependent behaviour is evident. Although the change in the width of the formed shear bands is less noticeable than in the biaxial test (Fig. 7), the magnitude of deviatoric strains increases as the size of the elements is reduced. The material points experience higher accelerations for the finer meshes, resulting in significantly larger displacements. The latter can be further identified in Fig. 12, where the evolution of the vertical displacement at point A for the standard MPM is shown. The activation of the failure

mechanism, when displacements grow rapidly, takes place earlier as the element size is reduced, i.e. it is triggered by a lower g value. Displacements at the end of the simulation also increase significantly as the mesh is refined. Furthermore, for the two finer meshes, with l_{ele} of 0.071 m and 0.062 m, numerical convergence issues were encountered and the simulations were not completed. This is a typical outcome when simulating softening materials in non-regularised continuum-based numerical analyses (Mánica et al., 2022a). The fact that accelerations, and in turn final displacements, depend on the adopted mesh is particularly relevant in the context of the MPM. These kinds of numerical techniques are generally adopted to address deformations beyond the capabilities of standard FEM formulations, for instance, to study not only the trigger of a failure but the consequences that the failure will have in the surrounding area. Therefore, run-out distances should not depend on the resolution of the background mesh adopted.

Fig. 13 shows contours of deviatoric strains and the position of materials points obtained with the regularised MPM. Here, a length scale parameter $l_s = 0.4$ m was adopted. Although some differences can still be identified for different meshes, they are much smaller than for the standard MPM. This is also evident in Fig. 12, which also shows the evolution of displacement at point A for the regularised simulations. Larger differences are obtained for the analysis with $l_{\mathrm{ele}} = 0.1$ m. However, it is important to notice that this element size is somewhat larger than the maximum identified in the biaxial test simulations for the proper performance of the nonlocal regularisation, of $0.2 l_s$.

To further stress the importance of regularisation, Fig. 14 shows curves of deviatoric stress q vs. displacement magnitude at point B, obtained with both the standard and regularised MPM, where q is defined as

$$q = \frac{1}{\sqrt{2}} \sqrt{(\sigma_1 - \sigma_2)^2 + (\sigma_2 - \sigma_3)^2 + (\sigma_1 - \sigma_3)^2} \ . \tag{38}$$

The standard MPM resulted in a more brittle response and with very different paths followed between the different analyses. Furthermore, a point was reached where displacements no longer accumulate and the deviatoric stress increases again. This is attributed to the formed shear band slightly shifting its position, causing point B to be located outside, to the left of the shear band and, thus, remaining relatively
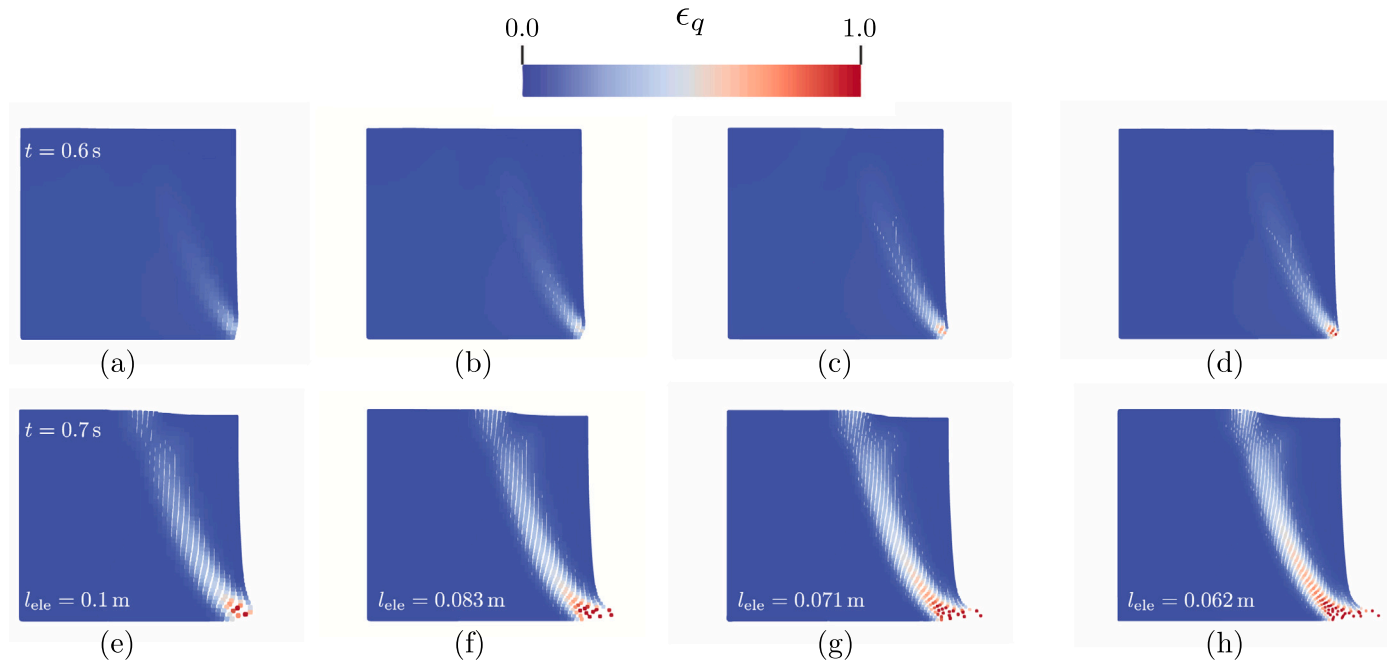
Fig. 13. Contours of normalised deviatoric strains and position of material points from the vertical cut simulation obtained with the regularised MPM, for times t of 0.6 and 0.7 s, using element sizes l_{ele} of (a,e) 0.1, (b,f) 0.083, (c,g) 0.071, and (d,h) 0.062 m.
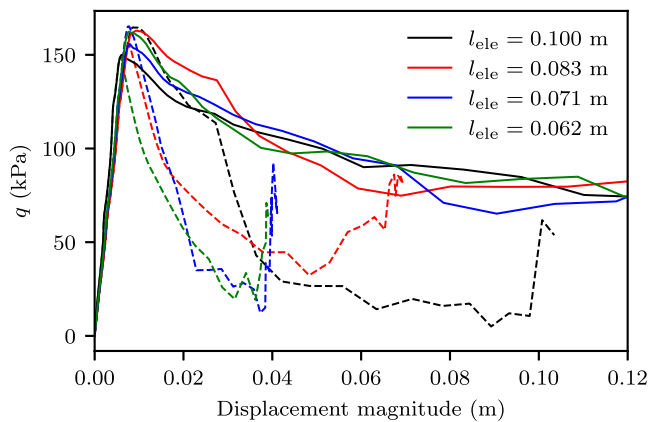

Fig. 14. Evolution of deviatoric stress at point B from the vertical cut simulation obtained with the standard (dashed lines) and regularised (solid line) MPM and for different element sizes l_{ele}.

Fig. 15. Geometry and boundary conditions of the shallow foundation simulation.

stationary during failure. In contrast, the regularised MPM resulted in similar curves regardless of the element size, showing a more or less monotonic reduction of q throughout the simulation.

4.3. Bearing capacity

The last benchmark, shown schematically in Fig. 15, corresponds to a stiff foundation that is pushed into the ground at a rate of $\Delta\delta = 2.5 \times 10^{-3}$ m per loading step. The interaction between the foundation and the ground is considered infinitely rough, hence no slippage occurs, ensuring that the foundation's movement into the soil is perfectly constrained against lateral displacement. Here, the static formulation is employed and, therefore, inertial forces are neglected. The adopted domain has a width and height of $w = 14$ and $h = 8$ m, respectively. At the bottom and lateral boundaries the displacements were fixed in the normal direction, while a null stress condition was considered at the
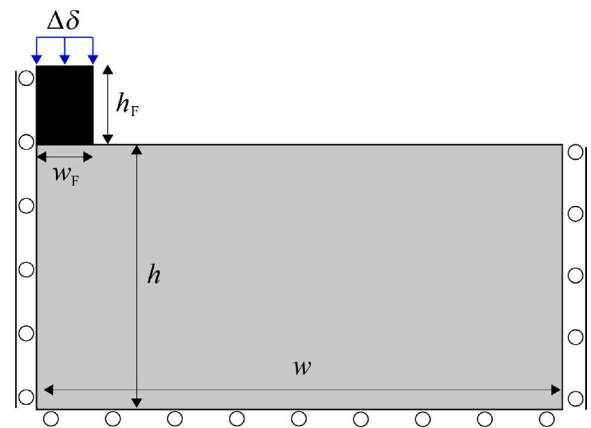
ground surface. The foundation has dimensions of $w_F = 1.5$ and $h_F = 3$ m. The adopted properties are listed in Table 1. Again, modifications with respect to the other benchmarks were made to obtain a marked failure mechanism for this BVP. For the regularised simulations, a length scale $l_s = 0.8$ m was employed.

Fig. 16 shows results in terms of normalised contours of deviatoric strains and the position of the material points, obtained with both the standard and regularised MPM and for different element sizes, after a foundation penetration of 0.3 m. All simulations exhibit similar results, with the formation of the classical Prandtl's failure mechanism. However, two notable differences can be identified for the standard MPM: (1) significantly larger deviatoric strains were developed and (2) an additional (vertical) shear path emerged below the bottom right corner of the foundation, with larger deviatoric strains as the element size is reduced. In the regularised simulations, this vertical shear band does not develop.

Differences between the standard and regularised simulations can also be identified in Fig. 17, which shows curves of the total deviatoric
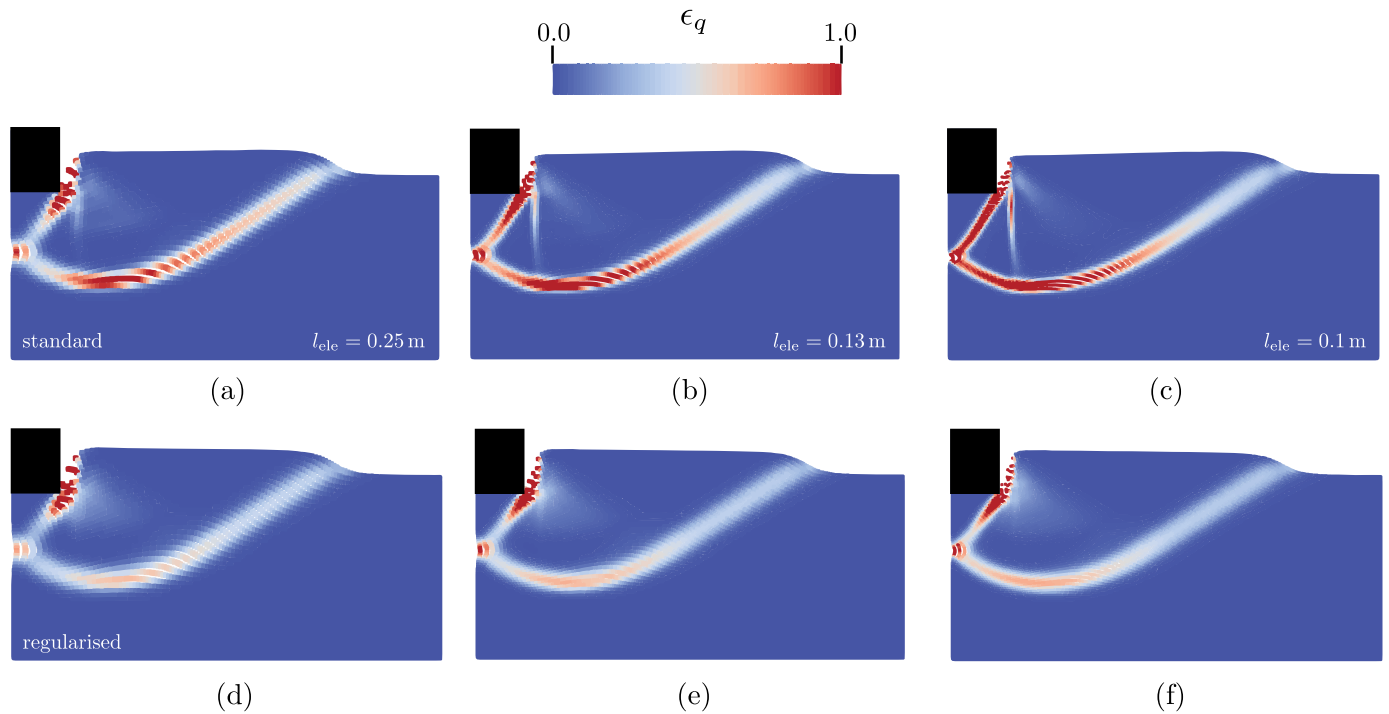
Fig. 16. Contours of normalised deviatoric strains and position of material points from the shallow foundation simulation obtained with the standard (top row) and regularised (bottom row) MPM using element sizes l_{ele} of (a, d) 0.25, (b, e) 0.13, and (c,f) 0.1 m.
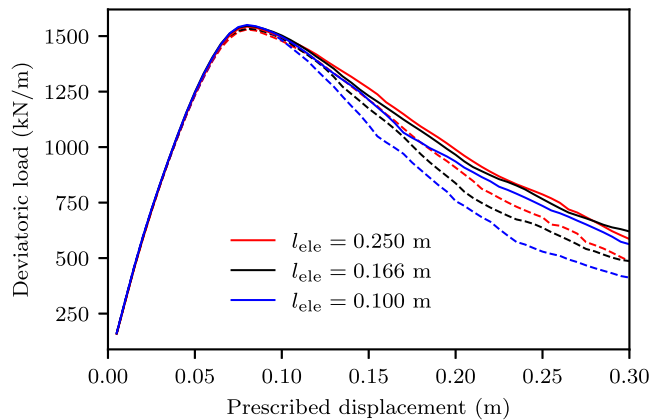

Fig. 17. Load vs. displacement curves from the shallow foundation simulation obtained with the standard (dashed lines) and regularised (solid lines) MPM and for different element sizes l_{ele}.

load vs. the prescribed vertical displacement of the foundation. All simulations reached a similar peak load. However, results from the standard MPM showed a more brittle response with a softening rate that increases as the element size is reduced. On the other hand, regularised simulations showed quite similar results, more or less independent of the adopted mesh. This is again significant for analyses of the whole failure process undertaken by MPM.

5. Conclusions

In this paper, a nonlocal regularisation was implemented into the MPM framework for the simulation of large deformation problems in brittle geomaterials. Unlike other nonlocal implementations in conventional FEM formulations, identification of neighbouring points, for the

computation of the nonlocal state variable, is performed at each global increment to account for the significant movement of material points. This identification was efficiently performed by taking advantage of the structured background mesh and a pre-established neighbourhood patch computed for each element. A number of benchmark simulations were carried out to demonstrate the importance of regularisation in MPM. However, an enhanced MPM formulation, namely the DM-GC MPM, was necessary since the well-known stress oscillation problem hindered a satisfactory analysis of the BVPs when dealing with softening materials. In general, the same numerical pathologies found in conventional FEM formulations were observed here. A more brittle response and larger strains and displacements are obtained for the non-regularised MPM as the size of elements is reduced. Furthermore, dynamic simulations showed that the run-out distance also depends on the adopted mesh, which is particularly relevant when using the MPM to study the consequences of a given collapse. On the other hand, regularised simulations showed consistent behaviour, with a global response and a configuration of localised deformations that are approximately independent of the employed mesh. However, in the case of the four-noded plane strain elements adopted here, the maximum element size with respect to the selected length scale parameter, for the proper performance of the nonlocal averaging, seems to be smaller than previous recommendations, in the order of $0.2 l_s$.

CRediT authorship contribution statement

José L. González Acosta: Writing – review & editing, Writing – original draft, Visualization, Validation, Software, Project administration, Methodology, Investigation, Formal analysis, Conceptualization. **Miguel A. Mánica:** Writing – review & editing, Writing – original draft, Visualization, Validation, Software, Project administration, Methodology, Investigation, Formal analysis, Conceptualization. **Philip J. Vardon:** Writing – review & editing. **Michael A. Hicks:** Writing – review & editing. **Antonio Gens:** Writing – review & editing.

Declaration of competing interest

The authors declare that they have no known competing financial interests or personal relationships that could have appeared to influence the work reported in this paper.

Data availability

No data was used for the research described in the article.

References

Anand, L., Aslan, O., Chester, S.A., 2012. A large-deformation gradient theory for elastic – plastic materials : Strain softening and regularization of shear bands. Int. J. Plast. 30–31, 116–143.

Bardenhagen, S.G., Kober, E.M., 2004. The generalized interpolation material point method. Comput. Model. Eng. Sci. 5 (6), 477–496.

Bathe, K.J., 1995. Finite Element Procedures, first ed. Prentice-Hall, Englewood Cliffs, NJ.

Bažant, Z.P., Jirásek, M., 2002. Nonlocal integral formulations of plasticity and damage: survey of progress. J. Eng. Mech. 128 (11), 1119–1149.

Bažant, Z.P., Lin, F.-B., 1988. Nonlocal yield limit degradation. Internat. J. Numer. Methods Engrg. 26 (8), 1805–1823.

Bažant, Z.P., Pijaudier-Cabot, G., 1988. Nonlocal continuum damage, localization instability and convergence. J. Appl. Mech. 55 (2), 287–293.

Benallal, A., Marigo, J.J., 2007. Bifurcation and stability issues in gradient theories with softening. Modelling Simul. Mater. Sci. Eng. 15 (1), S283–S295.

Bentley Systems, 2022. Plaxis CONNECT edition V22.01.

Beuth, L., Więckowski, Z., Vermeer, P.A., 2011. Solution of quasi-static large-strain problems by the material point method. Int. J. Numer. Anal. Methods Geomech. 35 (13), 1451–1465.

Brinkgreve, R.B.J., 1994. Geomaterials Models and Numerical Analysis of Softening (Ph.D. thesis). Delft University of Technology, p. 156.

Burghardt, J., Brannon, R., Guilkey, J., 2012. A nonlocal plasticity formulation for the material point method. Comput. Methods Appl. Mech. Engrg. 225, 55–64.

Burland, J.B., 1990. On the compressibility and shear strength of natural clays. Géotechnique 40 (3), 329–378.

Charlton, T., Coombs, W., Augarde, C., 2017. iGIMP: An implicit generalised interpolation material point method for large deformations. Comput. Struct. 190, 108–125.

Coombs, W.M., Charlton, T.J., Cortis, M., Augarde, C.E., 2018. Overcoming volumetric locking in material point methods. Comput. Methods Appl. Mech. Engrg. 333, 1–21.

Cui, W., Wu, X., Potts, D.M., Zdravković, L., 2023. Nonlocal strain regularisation for critical state models with volumetric hardening. Comput. Geotech. 157 (February).

de Borst, R., Sluys, L.J., Mühlhaus, H.-B., Pamin, J., 1993. Fundamental issues in finite element analysis of localization of deformation. Eng. Comput. 10 (2), 99–121, URL http://www.emeraldinsight.com/doi/10.1108/eb023897.

Desrues, J., Viggiani, G., 2004. Strain localization in sand: an overview of the experimental results obtained in grenoble using stereophotogrammetry. Int. J. Numer. Anal. Methods Geomech. 28 (4), 279–321.

Eringen, A.C., 1981. On nonlocal plasticity. Internat. J. Engrg. Sci. 19 (12), 1461–1474.

Eringen, A.C., 1983. Theories of nonlocal plasticity. Internat. J. Engrg. Sci. 21 (7), 741–751.

Frédéric, C., Panagiotis, K., Benoît, P., 2021. Numerical modeling of multiphysics couplings and strain localization. In: Instabilities Modeling in Geomechanics. John Wiley & Sons, Ltd, pp. 203–251, chapter 7. URL https://onlinelibrary.wiley.com/doi/abs/10.1002/9781119755203.ch7.

Galavi, V., Schweiger, H.F., 2009. A multilaminate model with destructuration. Soils Found. 49 (3), 341–353.

Galavi, V., Schweiger, H.F., 2010. Nonlocal multilaminate model for strain softening analysis. Int. J. Geomech. 10 (1), 30–44.

Gao, Z., Li, X., Lu, D., 2022. Nonlocal regularization of an anisotropic critical state model for sand. Acta Geotech. 17 (2), 427–439.

Gens, A., 2013. On the hydromechanical behaviour of argillaceous hard soils-weak rocks. In: Anagnostopoulos, A., Pachakis, M., Tsatsanifos, C. (Eds.), Proceedings of the 15th European Conference on Soil Mechanics and Geotechnical Engineering - Geotechnics of Hard Soils - Weak Rocks. Vol. 4, IOS Press, Athens, pp. 71–118, URL https://doi.org/10.3233/978-1-61499-199-1-71.

Gens, A., Carol, I., Alonso, E.E., 1990. A constitutive model for rock joints formulation and numerical implementation. Comput. Geotech. 9 (1–2), 3–20.

González Acosta, J.L., 2020. Investigation of MPM Inaccuracies, Contact Simulation and Robust Implementation for Geotechnical Problems (Ph.D. thesis). Delft University of Technology.

González Acosta, J.L., Vardon, P.J., Hicks, M.A., 2017. Composite material point method (CMPM) to improve stress recovery for quasi-static problems. Procedia Eng. 175, 324–331.

González Acosta, J.L., Vardon, P.J., Hicks, M.A., 2021a. Development of an implicit contact technique for the material point method. Comput. Geotech. 130, 103859.

González Acosta, J.L., Vardon, P.J., Hicks, M.A., 2021b. Study of landslides and soil-structure interaction problems using the implicit material point method. Eng. Geol. 285, 106043.

González Acosta, J.L., Vardon, P.J., Remmerswaal, G., Hicks, M.A., 2020. An investigation of stress inaccuracies and proposed solution in the material point method. Comput. Mech. 65 (2), 555–581.

González Acosta, J.L., Zheng, X., Vardon, P.J., Hicks, M.A., Pisano, F., 2019. On stress oscillation in MPM simulations involving one or two phases. In: Proceedings of the Second International Conference on the Material Point Method for Modelling Soil-Water-Structure Interaction. Cambridge, pp. 135–139.

Goodarzi, M., Rouainia, M., 2017. Modelling slope failure using a quasi-static MPM with a non-local strain softening approach. Procedia Eng. 175, 220–225.

Guilkey, J.E., Weiss, J.A., 2003. Implicit time integration for the material point method: Quantitative and algorithmic comparisons with the finite element method. Internat. J. Numer. Methods Engrg. 57 (9), 1323–1338.

Khoei, A.R., Karimi, K., 2008. An enriched-FEM model for simulation of localization phenomenon in cosserat continuum theory. Comput. Mater. Sci. 44 (2), 733–749.

Knuth, D.E., 1997. The Art of Computer Programming, third ed. Addison Wesley, Boston, MA.

Kohler, M., Stoecklin, A., Puzrin, A.M., 2022. A MPM framework for large-deformation seismic response analysis. Can. Geotech. J. 59 (6), 1046–1060.

Lian, Y., Zhang, X., Liu, Y., 2011. Coupling of finite element method with material point method by local multi-mesh contact method. Comput. Methods Appl. Mech. Engrg. 200 (47–48), 3482–3494.

Lu, X., Bardet, J.-P., Huand, M., 2012. Spectral analysis of nonlocal regularization in two-dimensional finite element models. Int. J. Numer. Anal. Methods Geomech. 36, 219–235, URL http://onlinelibrary.wiley.com/doi/10.1002/nag.527/abstract%5Cnhttps://web.natur.cuni.cz/uhigug/masin/download/MTVC_IJNAMG06-pp.pdf.

Mánica, M., 2018. Analysis of Underground Excavations in Argillaceous Hard Soils - Weak Rocks (Ph.D. thesis). Technical University of Catalonia.

Mánica, M.A., Ciantia, M.O., Gens, A., 2020. On the stability of underground caves in calcareous rocks due to long-term weathering. Rock Mech. Rock Eng. 53, 3885–3901.

Mánica, M.A., Gens, A., Vaunat, J., Armand, G., Vu, M.N., 2022a. Numerical simulation of underground excavations in an indurated clay using non-local regularisation. Part 1: formulation and base case. Geotechnique 72 (12), 1092–1112.

Mánica, M.A., Gens, A., Vaunat, J., Armand, G., Vu, M.N., 2022b. Numerical simulation of underground excavations in an indurated clay using non-local regularisation. Part 2: sensitivity analysis. Géotechnique 72 (12), 1113–1128.

Mánica, M.A., Gens, A., Vaunat, J., Ruiz, D.F., 2018. Nonlocal plasticity modelling of strain localisation in stiff clays. Comput. Geotech. 103, 138–150.

Marcher, T., 2003. Nichtlokale Modellierung der Entfestigung Dichter Sande und Steifer Tone (Ph.D. thesis). University of Stuttgart, p. 151.

Martinelli, M., Galavi, V., 2021. Investigation of the material point method in the simulation of cone penetration tests in dry sand. Comput. Geotech. 130, 103923.

Monforte, L., Ciantia, M.O., Carbonell, J.M., Arroyo, M., Gens, A., 2019. A stable mesh-independent approach for numerical modelling of structured soils at large strains. Comput. Geotech. 116.

Newmark, N.M., 1959. A method of computation for structural dynamics. J. Eng. Mech. Div. 85 (3), 67–94.

Phuong, N.T.V., Van Tol, A.F., Elkadi, A.S.K., Rohe, A., 2016. Numerical investigation of pile installation effects in sand using material point method. Comput. Geotech. 73, 58–71.

Pietruszczak, S., Mroz, Z., 1981. Finite element analysis of deformation of strain-softening materials. Internat. J. Numer. Methods Engrg. 17 (3), 327–334.

Read, H.E., Hegemier, G.A., 1984. Strain softening of rock, soil and concrete - a review article. Mech. Mater. 3 (4), 271–294.

Rolshoven, S., 2003. Nonlocal Plasticity Models for Localized Failure (Ph.D. thesis). École Polytechnique Fédérale de Lausanne.

Romero, T., Mánica, M.A., Ovando-Shelley, E., Rodríguez-Rebolledo, J.F., Buritica, J.A., 2024. On the determination of softening parameters for nonlocal constitutive models. J. Geotech. Geoenviron. Eng. submitted for publication.

Singh, V., Stanier, S., Bienen, B., Randolph, M.F., 2021. Modelling the behaviour of sensitive clays experiencing large deformations using non-local regularisation techniques. Comput. Geotech. 133, 104025.

Sluys, L.J., de Borst, R., 1992. Wave propagation and localization in a rate-dependent cracked medium-model formulation and one-dimensional examples. Int. J. Solids Struct. 29 (23), 2945–2958.

Summersgill, F.C., Kontoe, S., Potts, D.M., 2017. Critical assessment of nonlocal strain-softening methods in biaxial compression. Int. J. Geomech. 17 (7), 1–14.

Tejchman, J., Bauer, E., 2005. FE-simulations of a direct and a true simple shear test within a polar hypoplasticity. Comput. Geotech. 32 (1), 1–16.

Tielen, R., Wobbes, E., Möller, M., Beuth, L., 2017. A high order material point method. Procedia Eng. 175, 265–272.

Troncone, A., Pugliese, L., Conte, E., 2022. Analysis of an excavation-induced landslide in stiff clay using the material point method. Eng. Geol. 296, 106479.

van Eekelen, H.A.M., 1980. Isotropic yield surfaces in three dimensions for use in soil mechanics. Int. J. Numer. Anal. Methods Geomech. 4 (1), 89–101.

Vermeer, P.A., Brinkgreve, R.B.J., 1994. A new effective non-local strain measure for softening plasticity. In: Chambon, R., Desrues, J., Vardoulakis, I. (Eds.), Localisation and Bifurcation Theory for Soils and Rock. Balkema, Rotterdam, pp. 89–100.

Wang, B., Vardon, P.J., Hicks, M.A., Chen, Z., 2016. Development of an implicit material point method for geotechnical applications. Comput. Geotech. 71, 159–167.

Yerro, A., Girardi, V., Martinelli, M., Ceccato, F., 2022. Modelling unsaturated soils with the material point method. A discussion of the state-of-the-art. Geomech. Energy Environ. 32, 100343.

Yerro, A., Soga, K., Bray, J., 2019. Runout evaluation of oso landslide with the material point method. Can. Geotech. J. 56 (9), 1304–1317.

Zhang, F., Zhang, X., Sze, K.Y., Lian, Y., Liu, Y., 2017. Incompressible material point method for free surface flow. J. Comput. Phys. 330, 92–110.